

# Magnesium isotope evidence that accretional vapour loss shapes planetary compositions

Remco C. Hin<sup>1</sup>, Christopher D. Coath<sup>1</sup>, Philip J. Carter<sup>2†</sup>, Francis Nimmo<sup>3</sup>, Yi-Jen Lai<sup>1†</sup>, Philip A. E. Pogge von Strandmann<sup>1,4</sup>, Matthias Willbold<sup>1†</sup>, Zoë M. Leinhardt<sup>2</sup>, Michael J. Walter<sup>1</sup> & Tim Elliott<sup>1</sup>

**It has long been recognized that Earth and other differentiated planetary bodies are chemically fractionated compared to primitive, chondritic meteorites and, by inference, the primordial disk from which they formed. However, it is not known whether the notable volatile depletions of planetary bodies are a consequence of accretion<sup>1</sup> or inherited from prior nebular fractionation<sup>2</sup>. The isotopic compositions of the main constituents of planetary bodies can contribute to this debate<sup>3–6</sup>. Here we develop an analytical approach that corrects a major cause of measurement inaccuracy inherent in conventional methods, and show that all differentiated bodies have isotopically heavier magnesium compositions than chondritic meteorites. We argue that possible magnesium isotope fractionation during condensation of the solar nebula, core formation and silicate differentiation cannot explain these observations. However, isotopic fractionation between liquid and vapour, followed by vapour escape during accretionary growth of planetesimals, generates appropriate residual compositions. Our modelling implies that the isotopic compositions of magnesium, silicon and iron, and the relative abundances of the major elements of Earth and other planetary bodies, are a natural consequence of substantial (about 40 per cent by mass) vapour loss from growing planetesimals by this mechanism.**

Magnesium is a fundamental building block of the terrestrial planets, constituting around 15% of the mass of Earth. Compared to the ‘solar’ composition of the primordial disk, it is well established that the Earth is depleted in magnesium by approximately 20% relative to more cosmochemically refractory elements (for example, aluminium), consistent with increasing terrestrial depletions of elements with higher volatility (see, for example, ref. 7). Mass-dependent isotopic fractionations of other major elements, silicon and iron, have been used as evidence for compositional modification by accretional vapour loss<sup>3,6</sup>. Yet contrasting conclusions have been derived from similar observations in studies that point to fractionations occurring for these elements during planetary differentiation<sup>8,9</sup>. In this respect, the isotopic composition of magnesium may be better suited to interrogate chemical fractionation in the Solar System<sup>5</sup>. However, detecting mass-dependent isotopic differences between primitive chondrites and differentiated bodies poses considerable analytical challenges, because only small fractionations, much less than 1‰ per atomic mass unit (AMU), typically occur during the high-temperature processes (greater than 1,300 K) that shape planetary evolution. Indeed, various comparisons of terrestrial and chondritic magnesium isotope ratios have reached opposing conclusions as to whether the Earth is chondritic<sup>5,10–17</sup>. Much of the divergent opinion appears to stem from difficulties in achieving sufficiently accurate measurements<sup>18</sup>.

In Fig. 1a we illustrate that several different studies report chondritic <sup>25</sup>Mg/<sup>24</sup>Mg ratios that are around 0.03‰–0.05‰ lower than that of Earth<sup>5,10–12</sup>, but in only one case is Earth argued to be non-chondritic<sup>5</sup>. Reliable resolution of such small isotopic differences requires tight control of analytical artefacts. Of particular concern is that samples and standards behave slightly differently during analysis, despite prior purification. Unlike the traditional sample–standard bracketing approach, the method of double spiking explicitly corrects such behaviour, but it is not standard for elements with only three stable isotopes, such as magnesium. We have therefore developed an approach called ‘critical mixture double spiking’ to overcome this problem<sup>19</sup> (see Methods for details). On the basis of propagation of conservative estimates of systematic error, this method has a limiting accuracy of less than 0.005‰ per AMU (ref. 19). Repeat measurements of solution standards and geological reference materials indicate that we can achieve reproducibilities of ±0.010‰ (2 s.e.m.) on means comprising eight replicate measurements.

We measured the magnesium isotope compositions of a range of terrestrial rocks and primitive and differentiated meteorites using critical mixture double spiking (Table 1). As shown in Fig. 1b and c, our data substantiate the finding that chondrites have <sup>25</sup>Mg/<sup>24</sup>Mg ratios around 0.02‰ lower than the differentiated Earth, Mars, eucrite and angrite parent bodies.

Visual (Fig. 1b) and statistical (Methods) inspection show some data scatter. For terrestrial samples this is mostly due to two ocean island basalts, the sources of which probably contain recycled components, originally fractionated at the surface of the Earth. However, we focus on analyses of mantle peridotites to estimate the composition of the bulk Earth more robustly. Magnesium isotope variability among chondrites is foremost within the carbonaceous group. This scatter is readily explained by variable parent-body aqueous alteration, as their <sup>25</sup>Mg/<sup>24</sup>Mg ratios vary systematically with oxygen isotope compositions<sup>20</sup> and petrographic class (Extended Data Fig. 1) in the sense anticipated from terrestrial weathering<sup>21</sup>. Removing these anomalous samples, we document a statistically significant difference in magnesium isotope compositions between chondrites and the variably sized, differentiated bodies of Earth, Mars and the eucrite parent body ( $P_{\text{ANOVA}} = 1.5 \times 10^{-6}$ ; ANOVA, analysis of variance). If enstatite chondrites are considered separately from other chondrites ( $P_{\text{t-test}} = 0.017$ ), their mean <sup>25</sup>Mg/<sup>24</sup>Mg ratio is also significantly smaller than that of differentiated bodies (around 0.013‰;  $P_{\text{ANOVA}} = 7.8 \times 10^{-4}$ ). In contrast, the differentiated bodies are statistically indistinguishable from each other ( $P_{\text{ANOVA}} = 0.16$ ).

The lack of systematic differences in <sup>25</sup>Mg/<sup>24</sup>Mg ratios between melt-depleted harzburgites, fertile lherzolites and mid-ocean-ridge basalts reaffirm, at higher precision, previous observations<sup>12</sup> that

<sup>1</sup>School of Earth Sciences, University of Bristol, Wills Memorial Building, Queens Road, Bristol BS8 1RJ, UK. <sup>2</sup>School of Physics, University of Bristol, H. H. Wills Physics Laboratory, Tyndall Avenue, Bristol BS8 1TL, UK. <sup>3</sup>Department of Earth and Planetary Sciences, University of California, Santa Cruz, Santa Cruz, California 95064, USA. <sup>4</sup>London Geochemistry and Isotope Centre, Department of Earth Sciences, University College London, and Department of Earth and Planetary Sciences, Birkbeck, University of London, Gower Street, London WC1E 6BT, UK. <sup>†</sup>Present addresses: Department of Earth and Planetary Sciences, University of California, Davis, One Shields Avenue, Davis, California 95616, USA (P.J.C.); Macquarie University GeoAnalytical, Department of Earth and Planetary Sciences, Macquarie University, 12 Wally's Walk, Sydney, New South Wales 2109, Australia (Y.-J.L.); Geowissenschaftliches Zentrum Göttingen (GZG), University of Göttingen, Goldschmidtstrasse 1, 37077 Göttingen, Germany (M.W.).

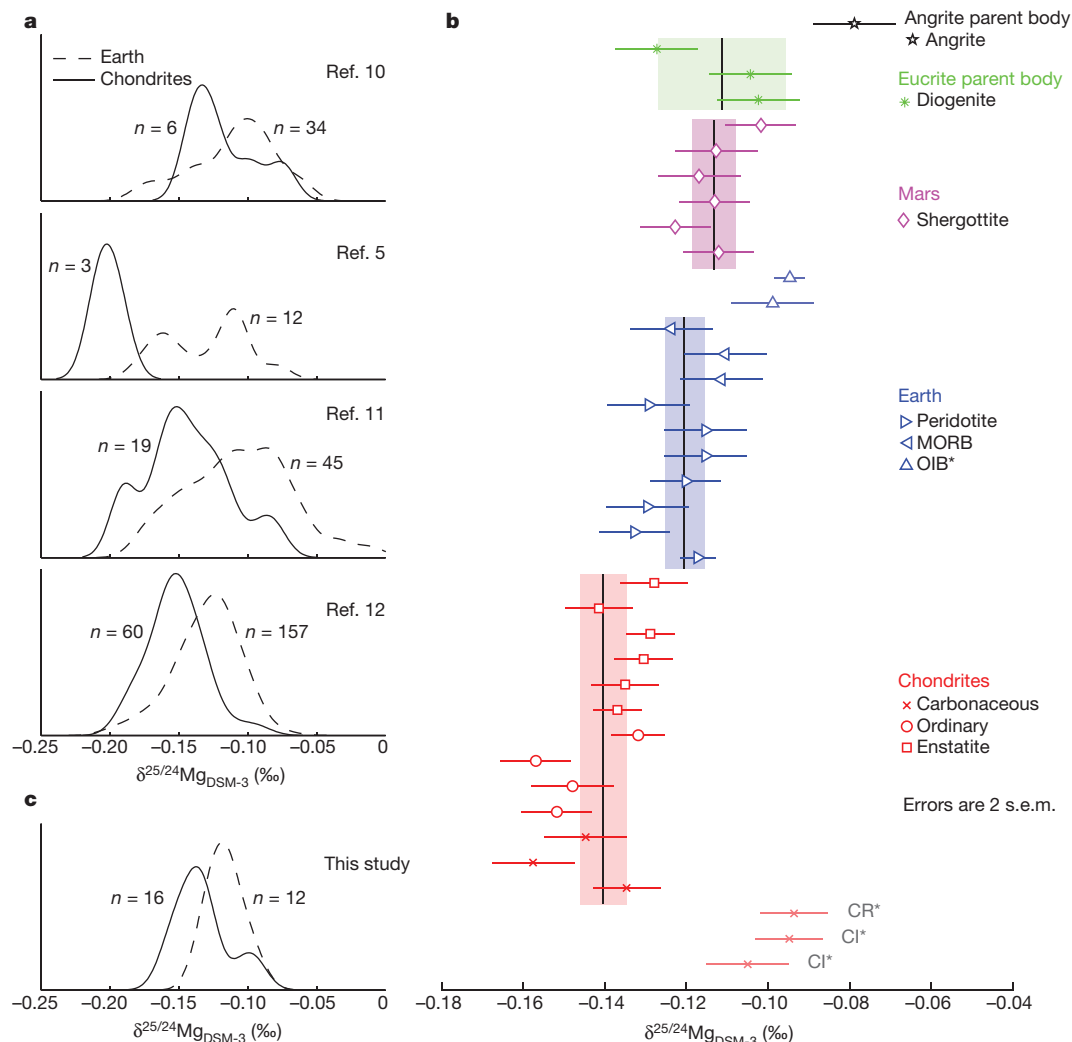


**Figure 1 | Magnesium isotope compositions expressed as relative deviations from the standard DSM-3,  $\delta^{25/24}\text{Mg}_{\text{DSM-3}}$ .** **a**, Probability density plots of magnesium isotope compositions from previous standard-sample bracketing work, highlighting the results of individual studies<sup>5,10–12</sup> that presented numerous analyses of both terrestrial and chondritic samples using the same methodology. These data show systematic, subtle differences (0.02‰–0.05‰) between the Earth and primitive meteorites.

magnesium isotopes do not fractionate discernibly during (ultra)mafic silicate differentiation (Fig. 1, Table 1 and Extended Data Fig. 2). Silicate differentiation is therefore not responsible for the relatively heavy magnesium isotope compositions of our samples of differentiated planetary bodies.

Although the difference in  $^{25}\text{Mg}/^{24}\text{Mg}$  ratio between Earth and primitive meteorites is small, bulk perturbation of such an abundant element requires the operation of planetary-scale processes. Core formation cannot account for this observation because, unlike iron and silicon, magnesium becomes siderophilic only at temperatures too high for substantial isotopic fractionation<sup>22</sup>. Vapour fractionation typically produces larger isotopic differences than do magmatic processes. Such fractionation may have occurred during the initial condensation of solids from the cooling proto-solar nebula, as has been invoked to explain variability between meteoritic and planetary silicon isotope compositions<sup>4</sup>. Yet, such a model predicts that enstatite chondrites, which have low Mg/Si ratios, should have the lowest  $^{25}\text{Mg}/^{24}\text{Mg}$  ratios of the primitive meteorites. This is inconsistent with our observations, in which enstatite chondrites have the isotopically heaviest Mg of the anhydrous chondrites, and moreover, the Earth is distinct from chondrites.

Typically authors refrained from interpreting such small differences. **b**, Samples from this study (measured by critical mixture double spiking) ordered according to sample type. Lines and shaded bars indicate means and 2 s.e.m. Samples displayed with pale symbols and marked with asterisks are excluded from means (see text). MORB, mid-ocean-ridge basalt; OIB, ocean island basalt. **c**, Earth and chondrite analyses from **b**, shown as a probability density plot to compare with **a**.

Instead, we propose that differentiated planetary bodies obtained their relatively heavy magnesium isotope compositions by vapour–melt fractionation following impacts during the accretionary growth of planetesimals. Loss of vapour, which was subsequently swept into the Sun or blown beyond the zone of accretion, would leave residual planetary bodies isotopically heavy. Vapour loss is most effective for bodies of less than about 0.1 Earth masses ( $M_{\oplus}$ ), as escape velocities of larger bodies are mostly too high to be exceeded by silicate vapour molecules (see Methods). We posit that signatures of vapour loss were imparted abundantly to small bodies in the inner Solar System, as evidenced by our analyses of silicate achondrites (Fig. 1b). Larger bodies such as Earth accreted dominantly from such vapour-depleted planetesimals, thereby inheriting their signatures.

Although small bodies can readily lose vapour, low mutual impact velocities limit the amount of vapour that is produced directly during these early stages of accretion. To investigate this quantitatively, we post-processed the results of previously published, high-resolution  $N$ -body simulations<sup>23</sup> (see Methods) using a parameterization of impact-induced vaporization<sup>4</sup>. In this model, cumulative vapour produced increases from less than 1% to about 20% of the final mass of a body, for bodies from  $10^{-4}M_{\oplus}$  to  $10^{-1}M_{\oplus}$  (Fig. 2a). As an alternative

**Table 1 | Magnesium isotope compositions of chondrites, terrestrial (ultra)mafic and achondrites**

Sample	Type	$\delta^{25/24}\text{Mg}_{\text{DSM-3}}$ (‰)	2 s.e.m.	<i>n</i> *
Orgueil	CI1	−0.105	0.010	8
Ivuna	CI1	−0.095	0.008	12
Al Rais	CR2	−0.094	0.008	12
Renazzo	CR2	−0.135	0.008	12
Kainsaz	CO3	−0.158	0.010	8
Murchison	CM2	−0.145	0.010	8
Parnallee	LL3	−0.152	0.009	11
Dhurmala	LL6	−0.148	0.010	8
Ceniceros	H3	−0.157	0.009	11
Zag	H3-6	−0.132	0.007	19, 2
Khairpur	EL6	−0.137	0.006	23, 2
Hvittis	EL6	−0.135	0.008	12
Yilmia	EL6	−0.130	0.007	16
St. Mark's	EH5	−0.129	0.006	23, 2
Abee	EH4	−0.142	0.008	12
Indarch	EH4	−0.128	0.008	12
Mean Chondrites†		−0.140	0.006	
JP-1	Dunite	−0.117	0.004	43, 5
BZ116	Sp Hz	−0.133	0.009	11
Vi 313-102	Gt Lz	−0.130	0.010	8
BZ143	Sp Lz	−0.120	0.009	11
BZ-29	Sp Lz	−0.115	0.010	8
Vi 314-56	Sp Lz	−0.115	0.010	8
BZ251	Plg Lz	−0.129	0.010	8
2370-1	MORB	−0.111	0.010	8
DS12-29	MORB	−0.110	0.010	8
9/30a(1)	MORB	−0.124	0.010	8
BIR-1	OIB	−0.099	0.010	8
BHVO-2	OIB	−0.095	0.004	60, 3
Mean Earth‡		−0.121	0.005	
ALHA 77005	Lz Sherg	−0.112	0.009	11
DaG 476	OI Sherg	−0.123	0.009	11
EETA 79001	Bas/OI Sherg	−0.113	0.009	11
RBT 04262	OI Sherg	−0.117	0.010	8
Zagami	Bas Sherg	−0.113	0.010	8
LAR 06319	OI Sherg	−0.102	0.009	11
Mean Mars		−0.113	0.006	
Johnstown	Diogenite	−0.102	0.010	8
Shalka	Diogenite	−0.104	0.010	8
Tatahouine	Diogenite	−0.127	0.010	8
Mean Diogenites		−0.111	0.016	
d'Orbigny	Angrite	−0.079	0.010	8

Sp Hz, spinel harzburgite; Gt Lz, garnet lherzolite; Plg, plagioclase; MORB, mid-ocean-ridge basalt; OIB, ocean island basalt; Bas Sherg, basaltic shergottite; OI, olivine-phyric.

\*Total number of analyses. If two numbers are listed, the second refers to the number of digestions. Each digestion was purified by ion exchange chromatography.

†The two CI1 chondrites (Ivuna, Orgueil) and one CR2 (Al Rais) were excluded from the mean.

‡The two ocean island basalts (BHVO-2 and BIR-1) were excluded from the mean.

approach, we have calculated vapour mass loss by direct outflow of silicate vapour from the surface of impact-generated magma ponds or oceans (see Methods). Although magma oceans may have been produced by radiogenic heating (for example,  $^{26}\text{Al}$  decay), we focused conservatively on converting impact velocities of the same *N*-body simulations to energy available for melting and vapour outflow. We obtain cumulative vapour mass losses of about 4% to 36% for bodies with final masses of  $10^{-4}M_{\oplus}$  to  $10^{-1}M_{\oplus}$  (Fig. 2b). Given the higher mass losses from smaller bodies in the second, magmatic scenario, we focus on this process.

The outflow velocities of vapour above the magma ponds or oceans are sufficiently high that this mechanism is not mass-discriminative. This implies that isotopic fractionation occurs only during production of vapour at the surface of the magma pond or ocean. We treat this as an equilibrium process between a molten surface and a transient atmosphere, as vapour–liquid chemical equilibrium is attained rapidly<sup>24</sup>. Furthermore, kinetic isotope fractionation in this scenario can be ruled out empirically, from consideration of predicted marked effects on potassium isotope ratios that are unobserved in nature<sup>25</sup> (see Methods).

We modelled magnesium, silicon and iron equilibrium isotope fractionation between liquid and vapour, with compositions calculated using thermodynamic data for a nine-component system of major and minor elements of variable volatility (see Methods). To obtain a residual planetesimal with a magnesium isotope composition around 0.02‰ higher than our chondritic values, our model predicts  $^{30}\text{Si}/^{28}\text{Si}$  and  $^{56}\text{Fe}/^{54}\text{Fe}$  ratios to be super-chondritic by approximately 0.30‰ and 0.013‰, respectively (Fig. 3a). These values are largely compatible with those for Earth (Fig. 3) and several other bodies (Extended Data Fig. 3), despite some rather poorly constrained input parameters (see Methods); refinement of these values may resolve these minor mismatches. Starting more specifically with an enstatite chondrite composition, as thought most isotopically appropriate for Earth (see, for example, ref. 26), about 47% of the body is vaporized and lost, which removes about 14% of the initial Mg mass together with about 65% Si, 48% Fe and more than 99.9% of Na and K (Fig. 3c). Similar total mass losses were deduced previously for Earth<sup>27</sup> from the volatilities of major constituents on the basis of a comparison to vaporization experiments. The total mass losses inferred from these chemical constraints (Fig. 3) are reassuringly similar to those calculated from our physical model of vapour loss (Fig. 2b).

The predicted elemental losses modify the composition of enstatite chondrites into one similar to that of Earth (Fig. 3c, d), without requiring substantial, preferential collisional erosion of a putative crust formed by a small degree of melting of an undifferentiated body<sup>28</sup>. Our modelled vapour loss modification resolves the conundrum that

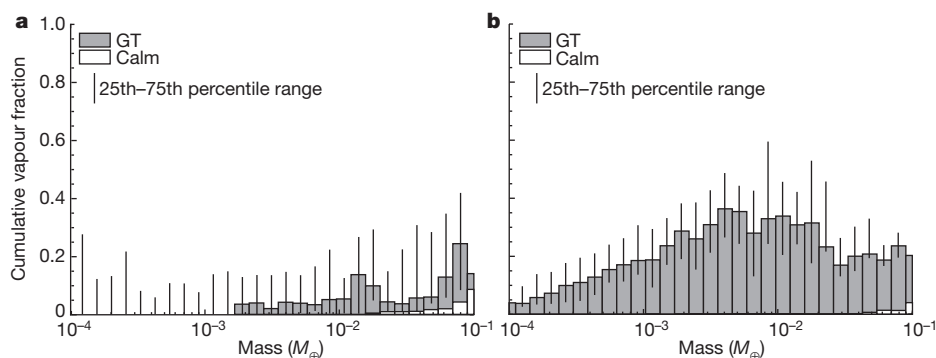


**Figure 2 | Median cumulative vapour fractions as a function of final planetary mass.** Values determined from high-resolution *N*-body simulations of planetary accretion<sup>23</sup>. The *N*-body simulations encompassed two scenarios: a calm disk without gas drag ('calm') and a disk that is disturbed by a Grand Tack motion of Jupiter<sup>30</sup> ('GT'). Final planetary masses are in Earth masses. **a**, Produced vapour fractions

calculated for impact vaporization parameterized to impact velocity<sup>4</sup>. **b**, Vapour loss fractions produced by direct outflow above exposed magma ponds or oceans. In a Grand Tack scenario, Jupiter's motions cause higher eccentricities and hence higher impact velocities for such small bodies, which explains their high vapour fractions.

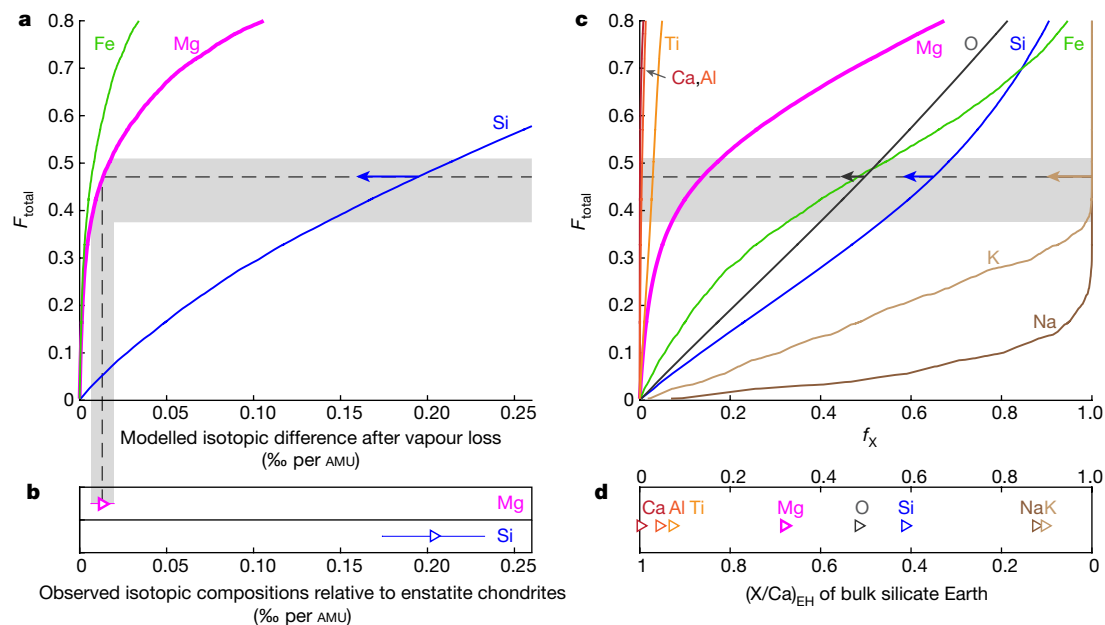


**Figure 3 | Comparison between modelled compositions of a vapour-depleted liquid and observed terrestrial compositions.** **a**, Changes in isotope compositions (‰ per AMU) against total relative vapour loss ( $F_{\text{total}}$ , in mole fractions) calculated in our model. **b**, Observed terrestrial Mg (this study), and Si (from ref. 4 and references therein) isotope compositions relative to enstatite chondrites. Errors are 2 s.e.m. **c**, Loss (mole fraction) of a given element ( $X$ ),  $f_X$ , versus  $F_{\text{total}}$ . **d**, Molar element/Ca ratio of the terrestrial mantle<sup>7</sup>, normalized to that of enstatite chondrites<sup>31</sup> ( $(X/\text{Ca})_{\text{EH}}$ ). Shaded bands give error bounds for  $F_{\text{total}}$  inferred from Mg isotope data.

the isotopic anomalies of Earth suggest a close link to enstatite chondrites, despite strikingly different elemental compositions<sup>26</sup>. However, close matches to the composition of the Earth are also obtained when starting with, for example, a CI chondrite composition (Extended Data Fig. 4). Although potassium depletion relative to chondrites in eucrite (>94%) and angrite (>99%) parent bodies<sup>25</sup> is comparable to our vapour depletion model results, it requires re-accretion of about 20% chondritic material to match terrestrial alkali abundances. This material can be derived from the distribution tail of bodies that escape melting and vapour loss.

Our vapour loss model quantitatively accounts for non-chondritic abundances and isotopic compositions of major elements as a natural consequence of planetary accretion, and provides a viable mechanism for previous suggestions of the importance of evaporative losses in planetary evolution<sup>3,6,27,29</sup>. This process inevitably results in a marked loss of elements more volatile than magnesium. Planetary compositions thus intrinsically reflect their history of collisional formation.

**Online Content** Methods, along with any additional Extended Data display items and Source Data, are available in the online version of the paper; references unique to these sections appear only in the online paper.

Received 29 November 2016; accepted 4 August 2017.

- Ringwood, A. E. Chemical evolution of the terrestrial planets. *Geochim. Cosmochim. Acta* **30**, 41–104 (1966).
- Anders, E. Chemical processes in the early Solar System, as inferred from meteorites. *Acc. Chem. Res.* **1**, 289–298 (1968).
- Pringle, E. A., Moynier, F., Savage, P. S., Badro, J. & Barrat, J. A. Silicon isotopes in angrites and volatile loss in planetesimals. *Proc. Natl Acad. Sci. USA* **111**, 17029–17032 (2014).
- Dauphas, N., Poitrasson, F., Burkhardt, C., Kobayashi, H. & Kurosawa, K. Planetary and meteorite Mg/Si and  $\delta^{30}\text{Si}$  variations inherited from solar nebula chemistry. *Earth Planet. Sci. Lett.* **427**, 236–248 (2015).
- Young, E. D., Tonui, E., Manning, C. E., Schauble, E. & Macris, C. A. Spinell–olivine magnesium isotope thermometry in the mantle and implications for the Mg isotopic composition of Earth. *Earth Planet. Sci. Lett.* **288**, 524–533 (2009).

The intersection of different curves with this field indicates the range of terrestrial depletions predicted for our vapour loss model. Comparison of these predicted values to those calculated for Earth relative to an enstatite chondrite starting composition (**b** and **d**) is generally good, despite uncertainties in model input parameters (see Methods) and additional influences on observed values from nebular and core formation processes<sup>4,9</sup>. Left-pointing arrows show the effect of post-volatile loss accretion of 20% chondrite (EH).

- Poitrasson, F., Halliday, A. N., Lee, D. C., Levasseur, S. & Teutsch, N. Iron isotope differences between Earth, Moon, Mars and Vesta as possible records of contrasted accretion mechanisms. *Earth Planet. Sci. Lett.* **223**, 253–266 (2004).
- Palme, H. & O'Neill, H. S. C. in *The Mantle and Core*, Vol. 2 of Treatise on Geochemistry (ed. Carlson, R. W.) Ch. 2.01 (Elsevier-Pergamon, 2003).
- Weyer, S. *et al.* Iron isotope fractionation during planetary differentiation. *Earth Planet. Sci. Lett.* **240**, 251–264 (2005).
- Georg, R. B., Halliday, A. N., Schauble, E. A. & Reynolds, B. C. Silicon in the Earth's core. *Nature* **447**, 1102–1106 (2007).
- Bourdon, B., Tipper, E. T., Fitoussi, C. & Stracke, A. Chondritic Mg isotope composition of the Earth. *Geochim. Cosmochim. Acta* **74**, 5069–5083 (2010).
- Pogge von Strandmann, P. A. E. *et al.* Variations of Li and Mg isotope ratios in bulk chondrites and mantle xenoliths. *Geochim. Cosmochim. Acta* **75**, 5247–5268 (2011).
- Teng, F. Z. *et al.* Magnesium isotopic composition of the Earth and chondrites. *Geochim. Cosmochim. Acta* **74**, 4150–4166 (2010).
- Wiechert, U. & Halliday, A. N. Non-chondritic magnesium and the origins of the inner terrestrial planets. *Earth Planet. Sci. Lett.* **256**, 360–371 (2007).
- Bizzarro, M. *et al.* High-precision Mg-isotope measurements of terrestrial and extraterrestrial material by HR-MC-ICPMS—implications for the relative and absolute Mg-isotope composition of the bulk silicate Earth. *J. Anal. At. Spectrom.* **26**, 565–577 (2011).
- Handler, M. R., Baker, J. A., Schiller, M., Bennett, V. C. & Yaxley, G. M. Magnesium stable isotope composition of Earth's upper mantle. *Earth Planet. Sci. Lett.* **282**, 306–313 (2009).
- Chakrabarti, R. & Jacobsen, S. B. The isotopic composition of magnesium in the inner Solar System. *Earth Planet. Sci. Lett.* **293**, 349–358 (2010).
- Yang, W., Teng, F. Z. & Zhang, H. F. Chondritic magnesium isotopic composition of the terrestrial mantle: a case study of peridotite xenoliths from the North China craton. *Earth Planet. Sci. Lett.* **288**, 475–482 (2009).
- Teng, F. Z. *et al.* Interlaboratory comparison of magnesium isotopic compositions of 12 felsic to ultramafic igneous rock standards analyzed by MC-ICPMS. *Geochim. Geophys. Geosyst.* **16**, 3197–3209 (2015).
- Coath, C. D., Elliott, T. & Hin, R. C. Double-spike inversion for three-isotope systems. *Chem. Geol.* **451**, 78–89 (2017).
- Clayton, R. N. & Mayeda, T. K. The oxygen isotope record in Murchison and other carbonaceous chondrites. *Earth Planet. Sci. Lett.* **67**, 151–161 (1984).
- Tipper, E. T. *et al.* The magnesium isotope budget of the modern ocean: constraints from riverine magnesium isotope ratios. *Earth Planet. Sci. Lett.* **250**, 241–253 (2006).



22. O'Rourke, J. G. & Stevenson, D. J. Powering Earth's dynamo with magnesium precipitation from the core. *Nature* **529**, 387–389 (2016).
23. Carter, P. J., Leinhardt, Z. M., Elliott, T., Walter, M. J. & Stewart, S. T. Compositional evolution during rocky protoplanet accretion. *Astrophys. J.* **813**, (2015).
24. Fegley, B. & Schaefer, L. in *The Atmosphere – History* Vol. 6 of *Treatise on Geochemistry* (ed. Farquhar, J.) Ch. 6.3 (Elsevier, 2013).
25. Humayun, M. & Clayton, R. N. Potassium isotope cosmochemistry: genetic implications of volatile element depletion. *Geochim. Cosmochim. Acta* **59**, 2131–2148 (1995).
26. Javoy, M. *et al.* The chemical composition of the Earth: Enstatite chondrite models. *Earth Planet. Sci. Lett.* **293**, 259–268 (2010).
27. Young, E. D. Assessing the implications of K isotope cosmochemistry for evaporation in the preplanetary solar nebula. *Earth Planet. Sci. Lett.* **183**, 321–333 (2000).
28. Boujibar, A., Andraut, D., Bolfan-Casanova, N., Bouhifd, M. A. & Monteux, J. Cosmochemical fractionation by collisional erosion during the Earth's accretion. *Nat. Commun.* **6**, 8295 (2015).
29. Pringle, E. A. & Moynier, F. Rubidium isotopic composition of the Earth, meteorites, and the Moon: Evidence for the origin of volatile loss during planetary accretion. *Earth Planet. Sci. Lett.* **473**, 62–70 (2017).
30. Walsh, K. J., Morbidelli, A., Raymond, S. N., O'Brien, D. P. & Mandell, A. M. Populating the asteroid belt from two parent source regions due to the migration of giant planets—"The Grand Tack". *Meteorit. Planet. Sci.* **47**, 1941–1947 (2012).
31. Wasson, J. T. & Kallemeyn, G. W. Compositions of chondrites. *Phil. Trans. R. Soc. Lond. A* **325**, 535–544 (1988).

**Supplementary Information** is available in the online version of the paper.

**Acknowledgements** We thank the Natural History Museum in London, NASA (National Aeronautics and Space Administration), O. Nebel, D. Ionov, S. Nielsen, E. Takazawa, K. Sims, Y. Niu, R. Brooker and C. Robinson for supplying us with various samples. We acknowledge C. Bierson for his help with direct outflow vapour loss modelling. This study was funded by NERC grant NE/L007428/1 to T.E., C.D.C. and M.J.W., which was motivated by NE/C0983/1. ERC Adv Grant 321209 ISONEB further supported the work of T.E. and C.D.C. NERC grant NE/K004778/1 to Z.M.L. funded P.J.C.

**Author Contributions** All data presented were measured by R.C.H. R.C.H. and C.D.C. performed vapour–liquid modelling. P.J.C. was responsible for calculations relating to *N*-body simulations. F.N. modelled the direct outflow vapour loss mechanism. R.C.H. and T.E. wrote the manuscript. C.D.C., Y.-J.L., P.A.E.P.v.S. and M.W. were involved in measurements in the initial stages of this study. All authors read and commented on the manuscript.

**Author Information** Reprints and permissions information is available at [www.nature.com/reprints](http://www.nature.com/reprints). The authors declare no competing financial interests. Readers are welcome to comment on the online version of the paper. Publisher's note: Springer Nature remains neutral with regard to jurisdictional claims in published maps and institutional affiliations. Correspondence and requests for materials should be addressed to R.C.H. ([remco.hin@bristol.ac.uk](mailto:remco.hin@bristol.ac.uk)).

**Reviewer Information** *Nature* thanks F. Moynier and E. Young for their contribution to the peer review of this work.

## METHODS

**Chemical and analytical protocols, and data statistics.** No statistical methods were used to predetermine sample size.

Powdered samples were digested in cleaned Savillex PFA beakers with 3:1 ultra-pure  $\sim 15.5$  M  $\text{HNO}_3$  and  $\sim 28$  M HF. Before drying,  $\sim 0.5$  ml 7 M  $\text{HClO}_4$  was added to prevent precipitation of insoluble fluorides. At this stage, insoluble chromites were visible in some peridotites. They were separated from the supernatant and further digested in high-pressure acid digestion vessels (Anton Paar Asher) before being recombined with the rest of the digested sample. Similarly, graphite precipitates were removed from enstatite chondrites by transferring the samples into pre-cleaned BN crucibles that were placed in a muffle furnace at  $600^\circ\text{C}$ , making use of the phase transition of graphite to  $\text{CO}_2$  under these conditions. Following complete digestion, any remaining organic components were treated with  $\sim 15.5$  M  $\text{HNO}_3$  and 30%  $\text{H}_2\text{O}_2$ . Terrestrial samples generally weighed 2–15 mg, whereas larger meteorite samples were dissolved ( $\sim 7$ –150 mg, majority 60–100 mg; see Extended Data Table 1) to obtain representative samples.

Magnesium was separated from the sample matrix with Biorad AG50W-X12 cationic exchange resin and 2 M  $\text{HNO}_3$  eluent as described previously<sup>11</sup>. Yields were monitored and were  $>99.85\%$  for all analysed samples. Following separation, samples were dissolved in 0.3 M  $\text{HNO}_3$  and critically double-spiked (see below) for analyses on a Thermo Finnigan Neptune (s/n 1020) multi-collector inductively coupled plasma mass spectrometer (MC-ICPMS). A Savillex PFA nebuliser ( $30$ – $40\ \mu\text{l min}^{-1}$  uptake) aspirated the sample solution into an Elemental Scientific Inc. Apex HF introduction system before ionisation in the plasma. A combination of Jet sampler and H skimmer cones was used and Mg masses 24, 25 and 26 were collected in cups L4, centre and H4, respectively. The Neptune was further operated in medium resolution mode ( $M/\Delta M \geq 4000$ , 5%–95% peak height definition) with an off-peak centre mass ( $^{25}\text{Mg}$  mass of 24.979 instead of 24.986) to resolve any minor possible  $^{12}\text{C}^{14}\text{N}^+$  interferences on  $^{26}\text{Mg}^+$ . However, these interferences should be insignificant as they were observed to be only  $\sim 15$  p.p.m. of the  $^{26}\text{Mg}^+$  signal. This medium-resolution mode also improved signal-to-noise ratios, reducing total background signals to  $<2 \times 10^{-13}$  A. A  $10^{11}\ \Omega$ -feedback resistor was used in the amplifier connected to the centre cup, whereas  $10^{10}\ \Omega$  resistors were used on L4 and H4. Total Mg intensities of  $\sim 2 \times 10^{-9}$  A were measured at total Mg concentrations of  $\sim 2.5\ \mu\text{g ml}^{-1}$  for 168 s integration (20 cycles of 8.4 s), consuming  $\sim 185$  ng sample Mg per analysis in double-spiked samples.

A measurement sequence typically consisted of analysis of a mixture of double-spike and DSM-3 reference standard followed by three sample–double-spike mixtures, repeating until all samples were measured before starting this series again to make duplicate analyses of samples. Normally, double-spike–sample mixture measurements were repeated four times per sequence, in which a total of 9–17 samples were measured. Sequences were repeated in different analysis sessions over the course of the study to yield at least eight repeated analyses of each double-spike–sample mixture. All sample and standard analyses were preceded by a 240 s wash-out and an on-peak background measurement (168 s integration). The mean intensities of the latter were subtracted from the intensities of the sample or standard analysis that followed it. Additionally, three analyses of unspiked DSM-3 (the total intensity matched to the double-spike–sample mixtures) were performed before, after and in the middle of the sequence of double-spike–sample (or standard) mixtures. A 15 min wash-out was performed between these unspiked and spiked analyses, because the Mg isotope composition of the background greatly changes as a consequence of switching between spiked and unspiked analyses, which makes critical mixture double spiking more prone to added variability because of background corrections. In our analyses, background corrections usually affected the reported isotope compositions by  $<0.0005\%$ , which is well below the uncertainties of  $0.008\%$ – $0.010\%$ . Sequences typically took  $\sim 10$ – $20$  h.

Interferences by hydrides (that is,  $^{24}\text{MgH}^+$  on  $^{25}\text{Mg}^+$  and  $^{25}\text{MgH}^+$  on  $^{26}\text{Mg}^+$ ), which are difficult to fully resolve, as well as background Mg intensities were reduced by using a  $-1$  kV extraction voltage instead of the default  $-2$  kV. We observed that such a change in the extraction voltage reduces background  $^{24}\text{MgH}^+$  and  $^{25}\text{MgH}^+$  intensities by  $\sim 10$  times to  $\sim 500$  counts per second  $^{24}\text{MgH}^+$  in medium resolution. Simultaneously, the change in extraction voltage lowers background Mg intensities by  $\sim 4$ – $5$  times, although sample sensitivity is only reduced by  $<20\%$ . Applying an extraction weaker than  $-1$  kV further decreases backgrounds, but increasingly lowers sensitivity. We interpret these effects as evidence that the background signals are dominantly produced by liberation (with/without hydride) of Mg deposited at the back of the skimmer cone. This hypothesis is substantiated by the fact that progressively increasing Mg background intensities can be lowered by brief cleaning of the back of the skimmer cone with a droplet of dilute  $\text{HNO}_3$ . Moreover, background Mg isotope compositions are extremely light after mass bias correction with the same instrumental fractionation factor as for sample Mg, suggesting additional mass fractionation. Finally, we observed that hydride intensities increase over background only  $\sim 75$ -fold when Mg intensities are increased

$\sim 25,000$ -fold by introducing sample Mg. We thus estimate that the largest relative hydride intensity contribution to Mg ( $^{24}\text{MgH}^+/^{25}\text{Mg}^+$ ) is  $\sim 13$  p.p.m. Because we externally normalize samples to intensity matched DSM-3 standards (see ‘Critical mixture double spiking’), these hydride contributions are reduced to such small levels that they do not affect our reported isotope compositions.

Data in Table 1 are reported as relative differences of isotope ratios to the reference solution standard DSM-3<sup>32</sup> in delta notation following IUPAC recommendations<sup>33</sup>:  $\delta^{25/24}\text{Mg}_{\text{DSM-3}} = [(^{25}\text{Mg}/^{24}\text{Mg})_{\text{sample}} / (^{25}\text{Mg}/^{24}\text{Mg})_{\text{DSM-3}} - 1]$ . The data are presented in per mille and represent means of repeated analyses. Reported uncertainties are standard error of the mean (2 s.e.m.) calculated as  $2s/\sqrt{n}$ , in which  $n$  is the number of repeated analyses for the corresponding sample. Instead of using the standard deviation ( $s$ ) of a sample or a geological reference material (for example, BHVO-2,  $2s = 0.029\%$ ,  $n = 60$  from three digestions), we determined  $s$  by a homoscedastic approach, pooling over all reference materials, samples and DSM-3<sup>34</sup>. That is, after determining the sums of the squared deviations of  $n$  repeated measurements from their  $m$  sample (and reference material and DSM-3) means, these sums were themselves summed before dividing by the degrees of freedom ( $k$ ):

$$s^2 = \frac{1}{k} \sum_{i=1}^m \sum_{j=1}^{n_i} (x_{ij} - \bar{x}_i)^2$$

with

$$k = \left( \sum_{i=1}^m n_i \right) - m$$

We obtained  $2s = 0.029\%$  ( $k = 693$ ), and were justified in using this scheme because the  $n$  repeats of  $m$  samples passed the null hypothesis of a Bartlett’s test; that is, the  $m$  samples come from normal distributions with the same variance.

Group means (for example, Earth) and their 2 s.e.m. uncertainties are calculated directly from the relevant sample data in Table 1. Significances of group mean differences were determined with a one-way ANOVA or a two-sample Student’s  $t$ -test, again using the relevant data in Table 1. Within-group differences were investigated with a one-way ANOVA using sample repeat measurements.

**Critical mixture double spiking.** The analysis routine described above is broadly similar to previous studies performed by standard–sample bracketing. Our contribution to addressing previously observed inter-laboratory inconsistencies<sup>18</sup> resides in the novelty of adding a double-spike before mass-spectrometric analysis. As detailed elsewhere<sup>19</sup>, this technique of ‘critical mixture double spiking’ corrects for mass bias effects of residual matrix, eliminating the most plausible cause for the inter-laboratory inconsistencies. It helps to ensure that analyses are not only precise, but also accurate to within the quoted precision. In practice, we dissolved  $^{25}\text{MgO}$  and  $^{26}\text{MgO}$  spikes (purchased from Oak Ridge National Laboratory, batch numbers 217201 and 158690, respectively) and mixed them to produce a double-spike with  $^{24,25,26}\text{Mg}$  abundances of 0.30%, 6.27%, 93.43%, approximating those for an accuracy-optimized scenario (0%, 8.4%, 91.6%, respectively<sup>19</sup>). We calibrated this double-spike to reference solution standard DSM-3 following our suggested protocol<sup>19</sup>.

After ion exchange chemistry, we aliquoted a weight of separated Mg sufficient for at least 10 runs and mixed this with a weighed amount of double-spike estimated to yield a molar spike proportion of 0.5908 in the mixture. This is the critical mixing proportion for our double-spike composition. Before analysis, double-spike–sample mixtures were equilibrated at  $100^\circ\text{C}$  for 2–3 h in closed Savillex PFA autosampler vials. Subsequently, all samples were analysed once by MC-ICPMS in a short sequence to determine their deviation from the critical spike proportion. At this stage, the mixtures were rarely within our acceptable bound of  $\pm 0.5\%$  molar proportion from critical. On the basis of the documented sample and double-spike weights and the observed double-spike proportion, either sample or double-spike was added to the mixtures, followed by re-equilibration and another short analysis sequence. At this stage most mixtures were found to be within 0.5% from critical.

An estimate of the instrumental mass bias is required for critical mixture double spiking<sup>19</sup>. We obtained this estimate from the unspiked DSM-3 analyses in the analysis sequence by dividing the measured  $^{25/24}\text{Mg}$  by the reference  $^{25/24}\text{Mg}$  of 0.12663 (ref. 35). Although this can also be done on  $^{26/24}\text{Mg}$ , we find that  $^{25/24}\text{Mg}$  is a more reproducible indicator of mass bias because it is less affected by incomplete wash-out owing to the smaller contrast between the unspiked and spiked ratios. These instrumental mass bias factors were linearly or quadratically interpolated on the basis of the evolution of DSM-3–double-spike mixtures to obtain a close mass bias approximation for the sample–double-spike mixtures. Once the mass bias estimate was obtained, the analyses were run through a double-spike inversion routine, followed by a normalization of sample isotope compositions to DSM-3

isotope compositions (obtained from double-spike–DSM-3 mixtures) to correct for residual non-exponential mass fractionation in the instrument.

Our observations are that the mass bias rarely varies by more than 0.5‰ per AMU during a 20-h sequence and that this variation tends to be characterized by a smooth evolution. Therefore, we conservatively estimate that the interpolated mass bias is accurate to  $\leq 0.25\%$  per AMU. Combined with our criterion of double-spike proportions being  $\leq 0.5\%$  from critical, we calculate that our Mg isotope compositions should be accurate to better than 0.005‰ on  $^{25}\text{Mg}/^{24}\text{Mg}$  (ref. 19). Note that this accuracy estimate is distinct from the reported uncertainty, which is determined from the scatter of replicates.

We have also analysed United States Geological Survey (USGS) geological reference material BHVO-2 with a deviation from a critical spike proportion of  $-1\%$  (overspiked) and  $+1\%$  (underspiked). The means of these samples are  $-0.092\% \pm 0.007\%$  and  $-0.090\% \pm 0.007\%$ , respectively. They are hence not significantly different at this level of precision, giving further confidence that our  $\pm 0.5\%$  mixing bound is sufficiently tight for accurate results.

Previously published data measured on key reference samples scatter beyond their 2 s.e.m. uncertainties<sup>18</sup>. Assuming sample homogeneity, this scatter highlights the distinction between accuracy and precision, which cannot be assessed separately in the traditional standard–sample bracketing procedure used by those studies. Although some of the data may thus appear precise, they can still be inaccurate. By contrast, we have assessed that our new critical double spiking technique should be accurate within our quoted precision. Hence, application of our technique should reduce the scatter in potential future studies from that observed in Extended Data Fig. 5 to within the error bounds of the isotope ratios found in this study, assuming sample homogeneity. Nonetheless, much of the literature data has  $\delta^{25/24}\text{Mg}$  consistent with our critically double-spiked measurements at a  $\pm 0.25\%$  level (Extended Data Fig. 5).

**N-body collisional accretion simulations.** Our N-body collisional accretion simulations have previously been published<sup>23</sup> and the reader is referred to the original publication for model details. These simulations were ideally suited for our investigations because they included growth of planetary bodies from  $\sim 10^{-4}$  to  $\sim 10^{-1} M_{\oplus}$  with imperfect accretion. We used two different modes of the high resolution simulations<sup>23</sup>, which include (i) a calm disk, and (ii) the Grand Tack<sup>30</sup>. Although we did not modify the simulations in any manner, we extracted additional information (notably impact parameters) to compute accretional vapour loss by two different mechanisms: impact vaporization, and vapour mass loss by direct outflow above exposed magma ponds.

**Impact vaporization.** This information was obtained following published vapour fraction equations (assuming molten basalt as the target phase)<sup>4</sup>. The equations enabled the determination of vapour mass ( $M_{\text{vap}}$ ) as a fraction of the impactor mass ( $M_{\text{imp}}$ ) in each collision. The vapour mass fraction in each collision ( $f_{\text{vap}}$ ) was calculated from the impact velocity and angle ( $v_{\text{imp}}$  and  $\theta$ ), which we have obtained from the N-body simulations (correcting for the expanded radii that were used in these simulations to increase the collision rate):  $f_{\text{vap}} = M_{\text{vap}}(v_{\text{imp}} \sin \theta) / M_{\text{imp}}$ . The vapour fraction in each collision was subsequently integrated over all collisions a body experienced, taking into account that each planetesimal has its own collisional history, to obtain the fraction of material that experienced impact-induced volatilization relative to the total mass of a body:  $F = (1/M) \int_0^M f_{\text{vap}}(v_{\text{imp}} \sin \theta) dm$ .

This equation is modified from the original<sup>4</sup> by replacing the  $v_{\text{esc}}(m)$  term, which was a proxy for impact velocity, by the impact velocities ( $v_{\text{imp}}$ ) obtained in our N-body simulations. This replacement resulted in higher volatilization fractions in our study compared to ref. 4, particularly for the Grand Tack simulation in which higher impact velocities occur owing to dynamical excitation by Jupiter's migration. We obtained Fig. 2 by binning the results for  $F$  in groups of masses (relative to Earth's mass  $M_{\oplus}$ ) in each of the two simulation modes.

**Vapour mass loss by direct outflow above exposed magma ponds.** *Summary.* The overall picture is as follows. We use the impact information from the N-body collisional accretion simulations and let each impact generate a hemispheric pool of melt. Vapour forms above the melt pool, with a pressure determined by the melt pool temperature. The vapour escapes at a rate determined by its temperature and the gravity of the body. The melt pool is assumed to be convecting vigorously, keeping it isothermal, and it cools from the surface because of evaporation and radiative heat transfer. As the melt cools, the vapour pressure drops and the vapour mass loss rate decreases until it effectively stops.

This overall behaviour is described by an energy equation as follows:

$$m C_p \dot{T} = \dot{m} \left( \frac{GM}{R_s} + L_v \right) + A \sigma T_{\text{eff}}^4 \quad (1)$$

where the left-hand side denotes the energy source (secular cooling of the melt pool) and the right-hand side denotes the energy sinks (evaporative cooling, gravitational potential energy and radiative heat transfer). Here  $m$  is the mass of

the melt pool,  $C_p$  is its specific heat capacity,  $\dot{T}$  is the cooling rate of the melt pool,  $\dot{m}$  is the vapour mass loss rate,  $M$  is the mass of the body,  $R_s$  is its radius,  $G$  is the gravitational coefficient,  $L_v$  is the latent heat of vaporization,  $\sigma$  is Stefan's constant,  $T_{\text{eff}}$  is the effective radiating temperature of the melt pool and  $A$  is its surface area. We take  $C_p = 1,200 \text{ J kg}^{-1} \text{ K}^{-1}$ ,  $L_v = 5 \text{ MJ kg}^{-1}$  and the magma density and body bulk density to both be  $3000 \text{ kg m}^{-3}$ .

Below we describe the different energy sources and sinks, and our calculation methods, in more detail. We have deliberately tried to keep our approach relatively simple, but even so there are a large number of parameters, some of which are highly uncertain. That being the case, a more complicated model seems premature; our main aim is to demonstrate that vapour loss from melt ponds is a plausible mechanism for generating vapour mass loss, and thereby isotopic fractionation.

**Mass loss rate.** Atmospheres which have a gas thermal velocity comparable to the escape velocity of the body are vulnerable to loss by direct outflow<sup>36</sup>. For Earth-mass bodies the thermal velocity required is implausibly high (except perhaps for close-in 'roaster' planets that may occur in exoplanetary systems<sup>37</sup>) but for small bodies this requirement is less restrictive. The resulting outflow can be described by the equations of mass and momentum conservation:

$$\frac{1}{\rho} \frac{d\rho}{dr} + \frac{1}{v} \frac{dv}{dr} + \frac{2}{r} = 0 \quad (2)$$

$$\frac{1}{\rho} \frac{dP}{dr} + v \frac{dv}{dr} = - \frac{GM}{r^2} \quad (3)$$

where  $r$  is the radial coordinate,  $P(T)$ ,  $\rho(T)$  and  $v$  are the pressure, density and radial velocity of the gas and we are assuming spherical geometry. For an ideal gas we have  $R'T = P/\rho = v_s^2$  where  $R'$  is the gas constant divided by the molar mass,  $T$  is the gas temperature and  $v_s$  is the speed of sound. To close the system, we also need an energy equation. The simplest, which we will adopt here, is to assume an isothermal atmosphere with the temperature set by the melt pool surface temperature  $T$ . A more realistic description would be to assume a vapour-saturated atmosphere; it has been shown<sup>38</sup> that this latter system is actually well approximated by the isothermal description.

Under these assumptions, the gas will accelerate outwards until it reaches the 'sonic point' at which  $v = v_s$ . At this critical radius  $r_c$  the sonic velocity is half the local escape velocity, with

$$r_c = \frac{GM}{2R'T} = R_s \left( \frac{v_{\text{esc}}}{2v_s} \right)^2$$

and  $v_{\text{esc}}$  is the escape velocity at the body surface ( $r = R_s$ ). The atmospheric mass loss rate is then given by  $4\pi r_c^2 \rho(r_c) v_s$ . Given the surface density, equations (2) and (3) may then be integrated outwards to calculate  $\rho(r_c)$  and thus the mass loss rate. For small bodies,  $r_c$  may be equal to or less than  $R_s$ , in which case the mass loss rate is  $4\pi R_s^2 \rho(R_s) v_s$ . In our case the gas density at the surface  $\rho(r_s)$  is set by the vapour pressure of the melt pool. Because only the melt pool is losing vapour, we replace  $4\pi R_s^2$  with  $A$ , the melt pool area, in our mass loss calculations. We assume a molar mass of  $0.04 \text{ kg mol}^{-1}$ , appropriate for MgO or SiO.

Driving mass loss requires energy because of two effects (equation (1)): conversion of liquid to vapour takes latent heat, and removal of mass from the surface to large distances involves potential energy changes. We consider both these effects in more detail below.

**Secular cooling and radiative heat transfer.** Secular cooling of the melt pool provides the energy to drive mass loss. The melt pool is assumed isothermal (temperature  $T$ ) owing to vigorous convection. This temperature sets the gas vapour pressure at the surface. Here we take the vapour pressure to be given by the following empirical expression obtained from our thermodynamic liquid–vapour model (see below):

$$\ln P = -4.0041(\ln T)^3 + 88.788(\ln T)^2 - 639.3 \ln T + 1,480.23$$

where  $P$  is in bar.

An important aspect of our model is that the effective radiating temperature of the melt pool  $T_{\text{eff}}$  is lower than the temperature  $T$  that sets the gas vapour pressure and defines the internal temperature of the melt. This effect is observed at terrestrial lava lakes, where the surface temperature is typically many hundreds of kelvins cooler<sup>39</sup> than the measured subsurface magma temperature and that inferred from the gas equilibrium chemistry<sup>40</sup>. A similar effect is found at Io, where the majority of a lava lake's surface is at much lower temperatures than the expected magma temperature<sup>41</sup>.

The reason for this effect is that there is a thin conductive skin on top of the convecting magma, which is at a lower temperature than the material beneath.



To approximately describe this phenomenon, we set the heat flux conducted across this layer equal to the heat flux radiated from the top surface:

$$F = \frac{k(T - T_{\text{eff}})}{\delta} = \sigma T_{\text{eff}}^4$$

where  $k$  is the thermal conductivity and  $\delta$  is the skin thickness. This allows us to solve for  $T_{\text{eff}}$  given  $T$  and  $\delta$ . To calculate  $\delta$  we assume the convecting melt pool can be described by isoviscous convection<sup>42</sup>

$$\delta \approx 2 \left[ \frac{\kappa \eta}{\rho g \alpha (T - T_{\text{eff}})} \right]^{1/3}$$

At high temperatures, the dominant energy sink in equation (1) is evaporative cooling, because radiative heat loss increases as  $T^4$ , whereas mass loss (which depends on the vapour pressure) increases exponentially with  $T$ . Thus, the overall mass loss calculations are not particularly sensitive to the details of the radiative cooling calculations.

Here we take  $\alpha = 3 \times 10^{-5} \text{ K}^{-1}$ ,  $\eta = 10^3 \text{ Pa s}$ . The thermal conductivity  $k$  is taken to be  $3 \text{ W m}^{-1} \text{ K}^{-1}$ , which then specifies  $\kappa$ . For  $T = 1,400 \text{ K}$  and a 1,000-km-radius body we find  $T_{\text{eff}} = 853 \text{ K}$ , which is roughly consistent with terrestrial lava lake measurements<sup>39</sup>.

**Melt pool volume and temperature.** To calculate the melt pool volume and temperature we assume that the volume of material shocked to the maximum temperature (the isobaric core) is hemispherical and has a radius linearly proportional to the impactor radius:  $R_{\text{ic}} = f R_{\text{p}}$ , with  $f = 3$  following literature<sup>4,43</sup>. Assuming that some fraction of the kinetic energy of the impactor is consumed within this volume, the temperature change associated with impact is then given by

$$\Delta T = \frac{1}{C_p} \left[ \left( \frac{R_{\text{ic}}}{R_{\text{ic}}} \right)^3 \beta v_{\text{imp}}^2 - L_m \right] \quad (4)$$

where  $L_m$  is the latent heat of fusion,  $v_{\text{imp}}$  is the impact velocity (given by the  $N$ -body simulations) and  $\beta$  is a factor to account for energy delivered beyond the isobaric core. Here we take  $\beta = 0.5$  to provide a conservative estimate of the initial melt temperature. Inspection of this equation shows that a minimum velocity of about  $4.6 \text{ km s}^{-1}$  is required to initiate an appreciable loss of mass.

We assume that the pre-impact target material is at the solidus, here taken to be  $1,400 \text{ K}$ . The justification for doing so is that heating by  $^{26}\text{Al}$  will melt bodies that formed early enough (to be conservative, we ignore at this stage that such melting induced by  $^{26}\text{Al}$  heating could have led to vapour mass loss). Melt advection will rapidly cool the target to  $1,400 \text{ K}$ , but subsequent cooling (by conduction or solid-state convection) will be much slower. We also impose a maximum melt temperature of  $3,500 \text{ K}$ . This is approximately the temperature at which total silicate vaporization is achieved and the physics of mass loss will change. Imposing this cut-off will underestimate the total amount of mass loss.

Although the radius of the isobaric core is uncertain, varying  $f$  does not have a very large effect on our results, because of the trade-offs involved. A smaller isobaric core reduces the surface area and cooling timescale, but it increases the melt temperature (and thus the vapour pressure and the initial mass loss rate). By contrast, the difference between regular and Grand Tack accretion is marked. This is because the Grand Tack results in more dynamical excitation, and thus more energetic collisions.

Extended Data Fig. 6 plots the median impact velocity normalized to the escape velocity as a function of body radius. The biggest difference between a calm disk (without gas drag) and Grand Tack accretion is that the normalized impact velocities for large bodies are much bigger in the latter. Since no vapour loss happens below a particular cut-off velocity (equation (4)), it is clear that Grand Tack simulations will generate much more vapour loss. Increasing  $\beta$  to 1 causes only modest increases in the predicted mass loss for conventional accretion, because impact velocities are still generally below the cut-off value.

**Implementation.** Each body undergoes mass growth by collision; each collision may also lead to some mass loss via vapour outflow. For each impact, we calculate the initial melt pool mass and temperature as outlined in Methods section 'Melt pool volume and temperature'. The instantaneous mass loss rate is calculated as described in Methods section 'Mass loss rate'. Given the mass loss rate, the change in melt pool temperature is calculated according to equation (1). The temperature is updated accordingly and the cycle then repeats. The total mass lost is tracked.

A disadvantage of our approach is that the pre-history of impactors striking a target body is not recorded. Since these impactors have probably undergone mass loss of their own, our approach may underestimate the total fractional mass loss of the final body. To mitigate this problem, for the Grand Tack results we perform

a two-step calculation. In the first step we calculate the total mass loss for each body neglecting inheritance effects. We use these results to determine the median mass loss over all bodies within a particular final mass range. The median prior fractional mass loss  $\phi$  determined in this manner for the Grand Tack bodies is given by the following empirical formula:

$$\phi = 0.4 \times 10^{-5} R_s^{1.65} \exp(-0.65 \times 10^{-5} R_s^{1.65})$$

where  $R_s$  is in kilometres. We then re-run the calculations, this time assuming that each impactor has experienced prior mass loss on the basis of this median value. The results of both calculations are shown in Extended Data Fig. 7.

For the conventional accretion simulations without gas present in the disk ('calm disk') vapour loss is sufficiently small that we neglected this inheritance effect. Extended Data Fig. 7 plots the median fractional mass loss for all bodies in the Grand Tack accretion simulations. The simulations for a calm disk result in very limited mass loss, and only for the largest bodies (see Fig. 2b). By contrast, mass loss in the Grand Tack scenario is much more extensive.

**Vapour-liquid Mg isotope fractionation models.** We first consider a kinetic isotope fractionation scenario. For this, we modelled the elemental loss of Mg required to obtain  $\sim 0.02\%$  heavier Mg isotope compositions by a Rayleigh distillation process with an experimentally determined kinetic isotope fractionation factor<sup>44</sup> (referred to as  $\alpha^{25/24} \text{ Mg}_{\text{g/liq}}^{\text{kin}}$ ) of 0.9860. We obtained a relative mass loss of Mg by vaporization ( $f_{\text{Mg}}^{\text{vap}}$ ) of 0.14% from  $f_{\text{Mg}}^{\text{vap}} = 1 - \exp[\ln(6^{25/24} \text{ Mg} + 1) / (\alpha^{25/24} \text{ Mg}_{\text{g/liq}}^{\text{kin}} - 1)]$ . This is a very small mass loss, but we can expect much larger concomitant K mass losses, owing to its higher volatility. Although it is hard to quantify such K loss, we can estimate it from an equilibrium liquid-vapour model (see below), given that kinetic evaporative fluxes ( $J$ ) from a molten surface are proportional to their saturation vapour pressures as well as the elemental mass<sup>44</sup>. In the simplest scenario, that is, assuming a single vaporization event, we find 0.14% of Mg is vaporized at  $\sim 2,700 \text{ K}$ , at which temperature  $\sim 28\%$  of K occurs as vapour (all as atomic K). Using a published<sup>45</sup>  $\alpha^{40/39} \text{ K}_{\text{g/liq}}^{\text{kin}}$  of 0.9892 we obtain that  $^{41}\text{K}/^{39}\text{K}$  fractionates by  $\sim 7\%$ . This compares to  $< 2.7\% \pm 1\%$  observed fractionation in Solar System material<sup>25</sup>, underscoring the implausibility of kinetic fractionation.

We also examine an equilibrium liquid-vapour fractionation model. Vapour production results in isotopically light vapour and heavy liquid compositions, thus evolving a vapour depleted bulk planetesimal to isotopically heavier compositions. The composition of silicate vapour in equilibrium with a molten planetesimal was calculated with a thermodynamic model involving equilibrium reactions between silicate liquid and vapour species for nine elements: O, Na, Mg, Al, Si, K, Ca, Ti and Fe. The model is modified from the MAGMA code by Fegley and co-workers<sup>46,47</sup>. We followed the approach of these authors to non-ideal mixing in the silicate liquid (that is, assuming ideal mixing of complex oxide and silicate pseudo-components), used their tabulated thermodynamic data, and, like them, we assumed ideal mixing in the gas. Our approach differs from theirs in that we relaxed their constraint that oxygen-to-metal ratios in the gas must be identical to the original liquid. Instead, we used the ideal gas law to convert partial pressures of gas species to number of moles in order to enforce conservation of mass by simultaneously solving mass balance equations for the number of moles of each element. Hence, we have 66 equilibrium equations and 9 mass balance equations to solve for activities of 75 species. The disadvantage of our approach is that the ideal gas law adds one freely adjustable parameter in the form of the volume the gas can expand into. We have chosen to fix this volume such that vapour fractions between  $\sim 0.001$  and  $\sim 0.15$  were obtained between  $2,500 \text{ K}$  and  $3,500 \text{ K}$ . Such fractions are of similar orders of magnitude to the average vapour fraction produced in single collisions in the  $N$ -body simulations (note that an order of magnitude variation in the chosen volume leads to  $\sim 5$ -fold variation in the vapour fractions, but these changes do not affect our conclusions because their effect is counterbalanced by the number of 'collisions' that are run to obtain the observed Mg isotope composition; see below). To convert from activities of the liquid species to moles, which we need for the mass balance equations, we need one more variable, the total moles of all liquid species, bringing the number of unknowns to 76. However, there is the activity normalization constraint: the activities (that is, mole fractions) of liquid species must sum to 1. Hence, we have 76 constraints to solve for 76 variables. The code is easily expandable with extra elements and equilibrium reactions and is freely available from the authors upon request.

In our equilibrium liquid-vapour fractionation model, we used published reduced partition functions ( $\beta$ ) to approximate equilibrium Mg, Si and Fe isotope fractionation factors between silicate liquid and atomic silicate vapour. Experimental calibrations of equilibrium isotope fractionation factors between vapour and liquid do not exist to date. As values of  $\beta$  are currently unavailable for silicate liquid, we approximated them with those for forsterite crystals for Mg (ref. 48) and Si (ref. 49) and fayalite crystals for Fe (ref. 50). We used further



literature sources for  $\beta$  for other vapour species  $\text{MgO}_{(g)}$  (ref. 48),  $\text{FeO}_{(g)}$  (ref. 51) and  $\text{SiO}_{(g)}$  (refs 49 and 52). Relative abundances of species in mixed vapours, for example,  $\text{Mg}_{(g)}$  and  $\text{MgO}_{(g)}$ , were obtained from the thermodynamic model described above. A two-component mass balance relationship combining isotope compositions of the vapour (subscript 'g') and the remaining 'liquid' (subscript 'liq') were used to determine the offset relative to the original bulk composition (set to 0 for reference here) before loss of a vapour fraction ( $f_g$ ):

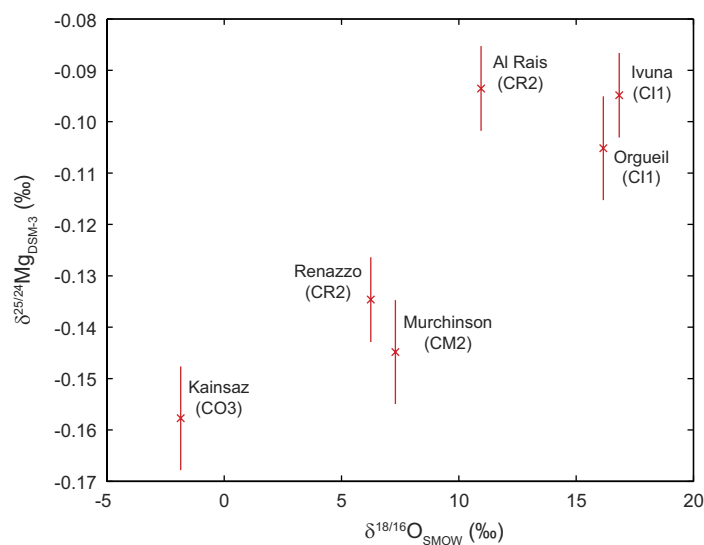
$$\delta^{25/24}\text{Mg}_{\text{liq}} = -f_g \delta^{25/24}\text{Mg}_g / (1 - f_g).$$

We used this equilibrium vapour–liquid fractionation model to simulate vapour loss after various temperature events (that is, planetary collisions). We initiated the model with a chondritic elemental composition (see main text) and isotope compositions ( $\delta^{25/24}\text{Mg}$ ) of 0, as mentioned above. We removed 95% of the chondritic Fe assuming it segregated into a core which is not affected by vaporization. We assumed that the silicate body undergoes full chemical homogenization between two events. After the first 'collision', the calculated isotopic and elemental compositions of the residual liquid were then used as initial values for the next 'collision', and so forth. The temperature used to calculate equilibrium vapour–liquid compositions and isotopic fractionation in any 'collision' event was obtained by random selection of a temperature uniformly distributed between 2,500 K and 3,500 K.

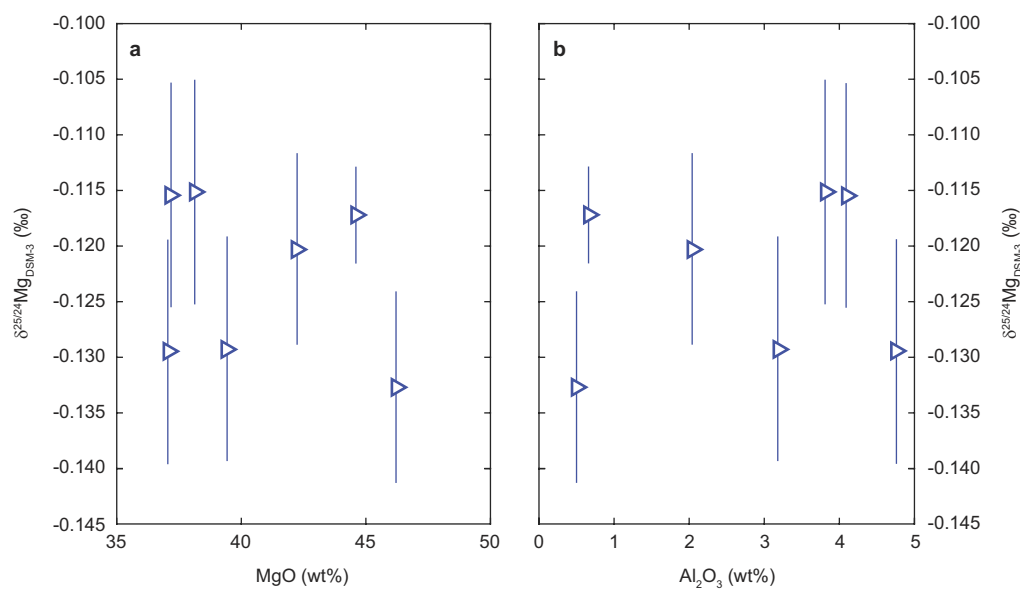
**Code availability.** The equilibrium liquid–vapour fractionation code and the code to calculate direct vapour outflow above exposed magma ponds are freely available from the corresponding author upon reasonable request. The N-body simulation code has restricted access, but output data and data processing code will be made available upon reasonable request to the corresponding author.

**Data availability.** Source Data for all figures not generated by modelling data have been provided with the paper. Data for Table 1 is provided as Supplementary Data. Data generated by modelling code can be obtained from the corresponding author upon reasonable request. Magnesium isotope compositions generated in this study are available in the EarthChem repository (<http://dx.doi.org/10.1594/IEDA/100713>).

32. Galy, A. *et al.* Magnesium isotope heterogeneity of the isotopic standard SRM980 and new reference materials for magnesium-isotope-ratio measurements. *J. Anal. At. Spectrom.* **18**, 1352–1356 (2003).
33. Coplen, T. B. Guidelines and recommended terms for expression of stable-isotope-ratio and gas-ratio measurement results. *Rapid Commun. Mass Spectrom.* **25**, 2538–2560 (2011).
34. Regelous, M., Elliott, T. & Coath, C. D. Nickel isotope heterogeneity in the early Solar System. *Earth Planet. Sci. Lett.* **272**, 330–338 (2008).
35. Catanzaro, E. J., Murphy, T. J., Garner, E. L. & Shields, W. R. Absolute isotopic abundance ratios and atomic weight of magnesium. *J. Res. Natl Bur. Stand. Sec. A* **70**, 453–458 (1966).
36. Pierrehumbert, R. T. *Principles of Planetary Climate* 555–564 (Cambridge University Press, 2010).
37. Perez-Becker, D. & Chiang, E. Catastrophic evaporation of rocky planets. *Mon. Not. R. Astron. Soc.* **433**, 2294–2309 (2013).
38. Lehmer, O. R., Catling, D. C. & Zahnle, K. J. The longevity of water ice on Ganymedes and Europas around migrated giant planets. *Astrophys. J.* **839**, 32–40 (2017).
39. Patrick, M. R., Orr, T., Swanson, D. A. & Lev, E. Shallow and deep controls on lava lake surface motion at Kilauea Volcano. *J. Volcanol. Geotherm. Res.* **328**, 247–261 (2016).
40. Moussallam, Y. *et al.* Hydrogen emissions from Erebus volcano, Antarctica. *Bull. Volcanol.* **74**, 2109–2120 (2012).
41. Davies, A. G. *Volcanism on Io: A Comparison with Earth* 187 (Cambridge Univ. Press, 2007).
42. Solomatov, V. S. Scaling of temperature- and stress-dependent viscosity convection. *Phys. Fluids* **7**, 266–274 (1995).
43. Melosh, H. J. *Impact Cratering: A Geologic Process* 62–63 (Oxford Univ. Press, 1989).
44. Richter, F. M., Janney, P. E., Mendybaev, R. A., Davis, A. M. & Wadhwa, M. Elemental and isotopic fractionation of type B CAI-like liquids by evaporation. *Geochim. Cosmochim. Acta* **71**, 5544–5564 (2007).
45. Richter, F. M., Mendybaev, R. A., Christensen, J. N., Ebel, D. & Gaffney, A. Laboratory experiments bearing on the origin and evolution of olivine-rich chondrules. *Meteorit. Planet. Sci.* **46**, 1152–1178 (2011).
46. Fegley, B. & Cameron, A. G. W. A vaporization model for iron/silicate fractionation in the Mercury protoplanet. *Earth Planet. Sci. Lett.* **82**, 207–222 (1987).
47. Schaefer, L. & Fegley, B. A thermodynamic model of high temperature lava vaporization on Io. *Icarus* **169**, 216–241 (2004).
48. Schauble, E. A. First-principles estimates of equilibrium magnesium isotope fractionation in silicate, oxide, carbonate and hexaaquamagnesium(2+) crystals. *Geochim. Cosmochim. Acta* **75**, 844–869 (2011).
49. Huang, F., Wu, Z. Q., Huang, S. C. & Wu, F. First-principles calculations of equilibrium silicon isotope fractionation among mantle minerals. *Geochim. Cosmochim. Acta* **140**, 509–520 (2014).
50. Polyakov, V. B. & Mineev, S. D. The use of Mössbauer spectroscopy in stable isotope geochemistry. *Geochim. Cosmochim. Acta* **64**, 849–865 (2000).
51. Pahlevan, K. *Chemical and Isotopic Consequences of Lunar Formation via Giant Impact*. PhD thesis, California Institute of Technology (2010).
52. Javoy, M., Balan, E., Méheut, M., Blanchard, M. & Lazzeri, M. First-principles investigation of equilibrium isotopic fractionation of O- and Si-isotopes between refractory solids and gases in the solar nebula. *Earth Planet. Sci. Lett.* **319**, 118–127 (2012).
53. Clayton, R. N. & Mayeda, T. K. Oxygen isotope studies of carbonaceous chondrites. *Geochim. Cosmochim. Acta* **63**, 2089–2104 (1999).
54. Van Schmus, W. R. & Wood, J. A. A chemical-petrologic classification for the chondritic meteorites. *Geochim. Cosmochim. Acta* **31**, 747–765 (1967).
55. Sossi, P. A., Nebel, O. & Foden, J. Iron isotope systematics in planetary reservoirs. *Earth Planet. Sci. Lett.* **452**, 295–308 (2016).
56. O'Neill, H. S. C. & Palme, H. Collisional erosion and the non-chondritic composition of the terrestrial planets. *Phil. Trans. R. Soc. Lond. A* **366**, 4205–4238 (2008).
57. Badro, J. *et al.* Effect of light elements on the sound velocities in solid iron: Implications for the composition of Earth's core. *Earth Planet. Sci. Lett.* **254**, 233–238 (2007).
58. Hin, R. C., Fitoussi, C., Schmidt, M. W. & Bourdon, B. Experimental determination of the Si isotope fractionation factor between liquid metal and liquid silicate. *Earth Planet. Sci. Lett.* **387**, 55–66 (2014).
59. Armytage, R. M. G., Georg, R. B., Savage, P. S., Williams, H. M. & Halliday, A. N. Silicon isotopes in meteorites and planetary core formation. *Geochim. Cosmochim. Acta* **75**, 3662–3676 (2011).
60. Schiller, M., Handler, M. R. & Baker, J. A. High-precision Mg isotopic systematics of bulk chondrites. *Earth Planet. Sci. Lett.* **297**, 165–173 (2010).
61. Schiller, M., Baker, J. A. & Bizzarro, M.  $^{26}\text{Al}$ – $^{26}\text{Mg}$  dating of asteroidal magmatism in the young Solar System. *Geochim. Cosmochim. Acta* **74**, 4844–4864 (2010).
62. Larsen, K. K. *et al.* Evidence for magnesium isotope heterogeneity in the solar protoplanetary disk. *Astrophys. J.* **735**, L37 (2011).
63. Takazawa, E., Frey, F. A., Shimizu, N. & Obata, M. Whole rock compositional variations in an upper mantle peridotite (Horoman, Hokkaido, Japan): are they consistent with a partial melting process? *Geochim. Cosmochim. Acta* **64**, 695–716 (2000).
64. Ionov, D. A., Ashchepkov, I. & Jagoutz, E. The provenance of fertile off-craton lithospheric mantle: Sr–Nd isotope and chemical composition of garnet and spinel peridotite xenoliths from Vitim, Siberia. *Chem. Geol.* **217**, 41–75 (2005).
65. Brooker, R. A., James, R. H. & Blundy, J. D. Trace elements and Li isotope systematics in Zabargad peridotites: evidence of ancient subduction processes in the Red Sea mantle. *Chem. Geol.* **212**, 179–204 (2004).
66. Sims, K. W. W. *et al.* Chemical and isotopic constraints on the generation and transport of magma beneath the East Pacific Rise. *Geochim. Cosmochim. Acta* **66**, 3481–3504 (2002).
67. Niu, Y. L. & Batiza, R. Magmatic processes at a slow-spreading ridge segment: 26°S Mid-Atlantic Ridge. *J. Geophys. Res.* **99**, 19719–19740 (1994).
68. Robinson, C. J., White, R. S., Bickle, M. J. & Minshull, T. A. Restricted melting under the very slow-spreading Southwest Indian ridge. *Geol. Soc. London Spec. Publ.* **118**, 131–141 (1996).

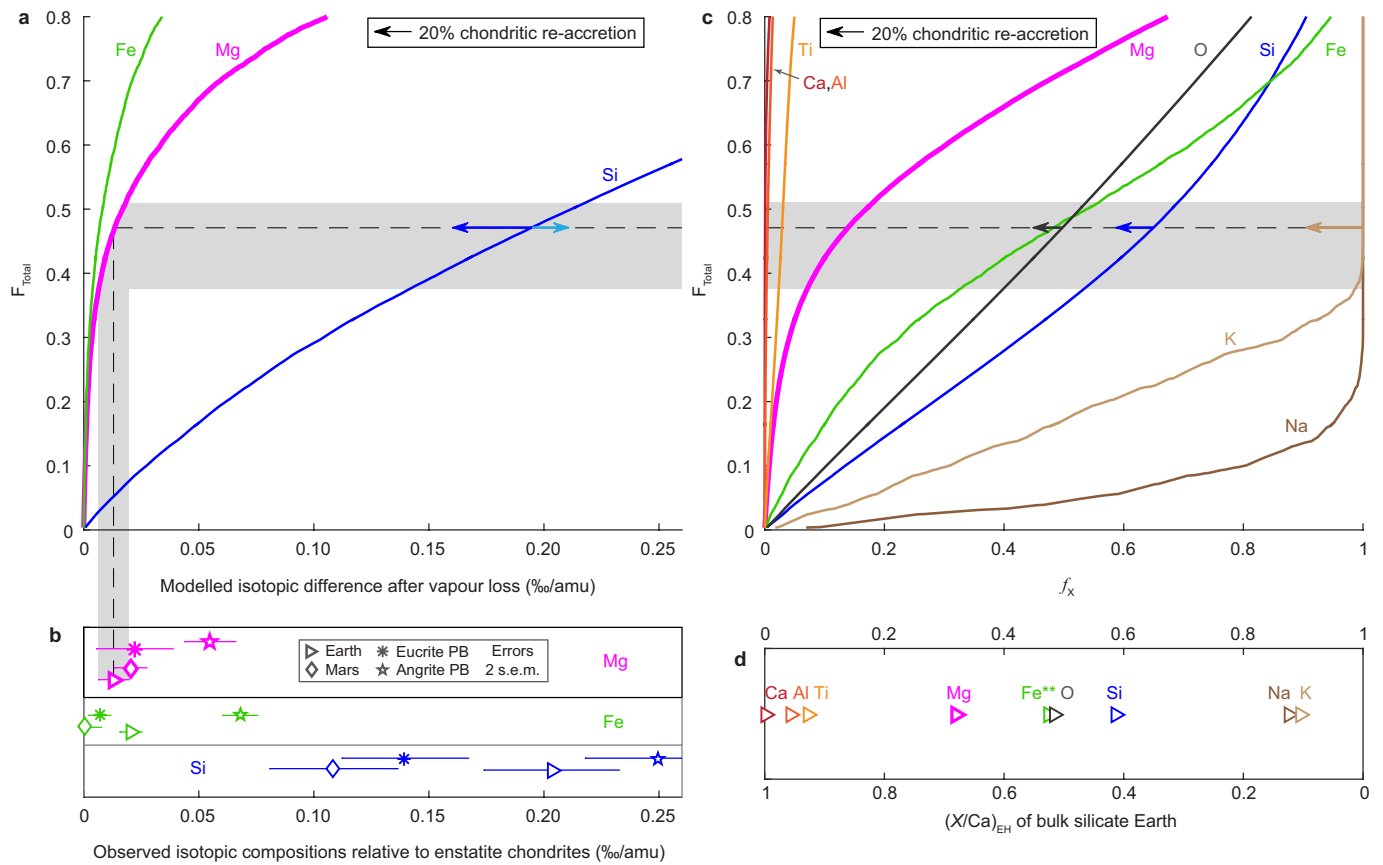


**Extended Data Figure 1 | Magnesium isotope compositions of carbonaceous chondrites.** The compositions are plotted against their average literature oxygen isotope compositions<sup>53</sup>. These mass-dependent oxygen isotope measurements reflect parent body hydrothermal alteration<sup>20</sup>, so the correlation ( $R^2 = 0.78$ ) between Mg and O isotopes (as well as with the petrographic group<sup>54</sup>, indicated in brackets under sample names) implies that the Mg isotope compositions of some carbonaceous chondrites have been altered by hydrothermal processes. The most altered samples, to the upper right of this diagram, are excluded from our chondrite Mg isotope means.



**Extended Data Figure 2 | Magnesium isotope compositions of terrestrial peridotites.** The compositions are plotted against whole rock MgO (**a**) and  $\text{Al}_2\text{O}_3$  (**b**) contents. The absence of correlations of Mg isotope compositions with MgO or  $\text{Al}_2\text{O}_3$  indicates the absence of discernible Mg isotope fractionation during partial melting.

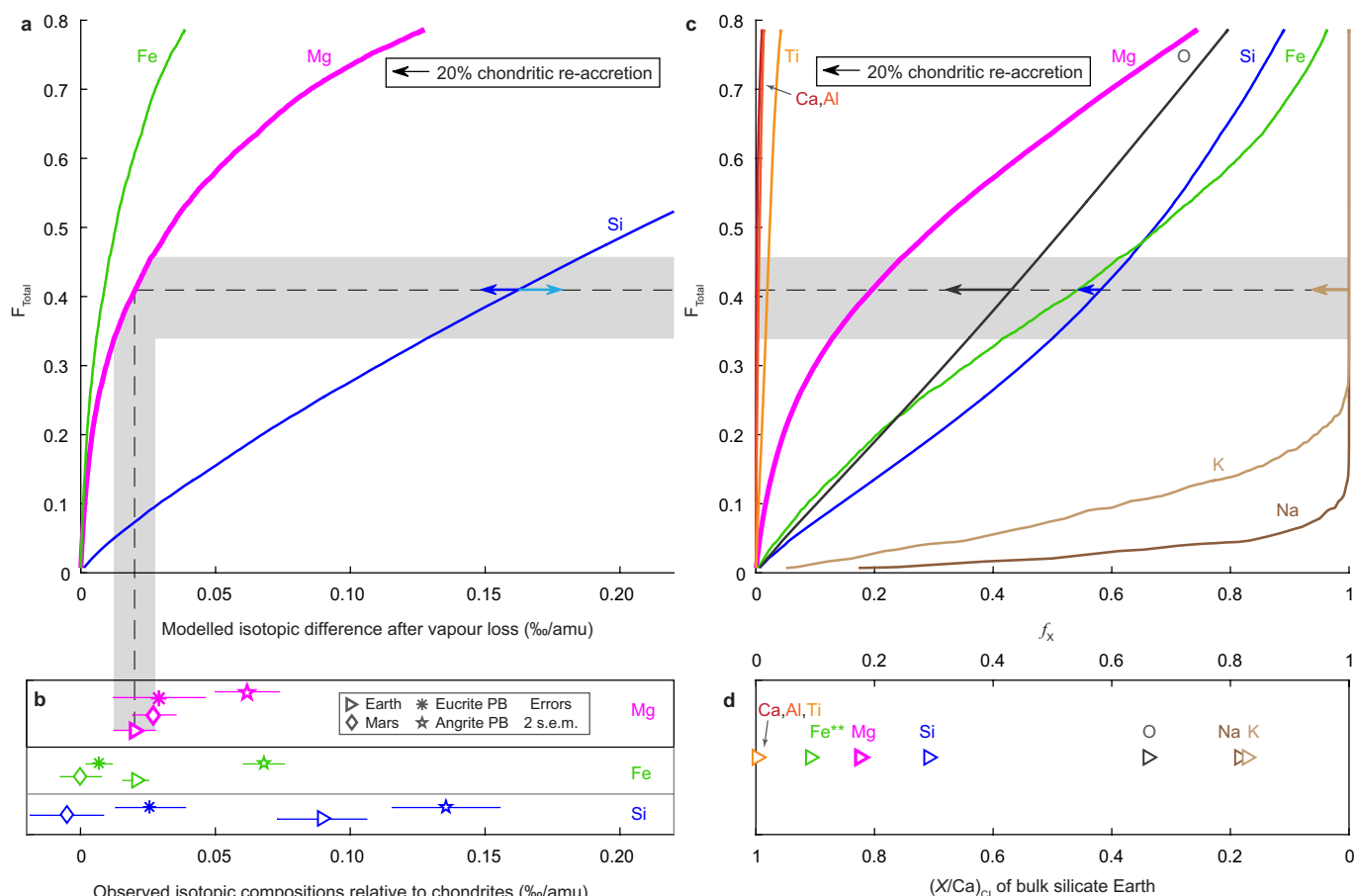




### Extended Data Figure 3 | Comparison between modelled compositions of a vapour-depleted liquid and observed planetary compositions.

As Fig. 3, showing **a**, Modelled changes in isotope compositions (‰ per AMU) against total relative vapour loss ( $F_{\text{Total}}$ , in mole fractions). **b**, Observed isotope compositions relative to enstatite chondrites (errors are 2 s.e.m.). **c**, Loss (mole fraction) of a given element ( $X$ ),  $f_x$ , versus  $F_{\text{Total}}$ . **d**, Molar element/Ca ratio of the terrestrial mantle<sup>7</sup>, normalized to that of enstatite chondrites<sup>31</sup> ( $(X/\text{Ca})_{\text{EH}}$ ). Compared to Fig. 3, observed isotope compositions for Mars, and eucrite and angrite parent bodies as well as elemental and isotopic Fe observations are additionally included (**b** and **d**; Fe isotope data from ref. 55 and references therein, all other references as in Fig. 3). Comparison of observed Fe contents and isotope

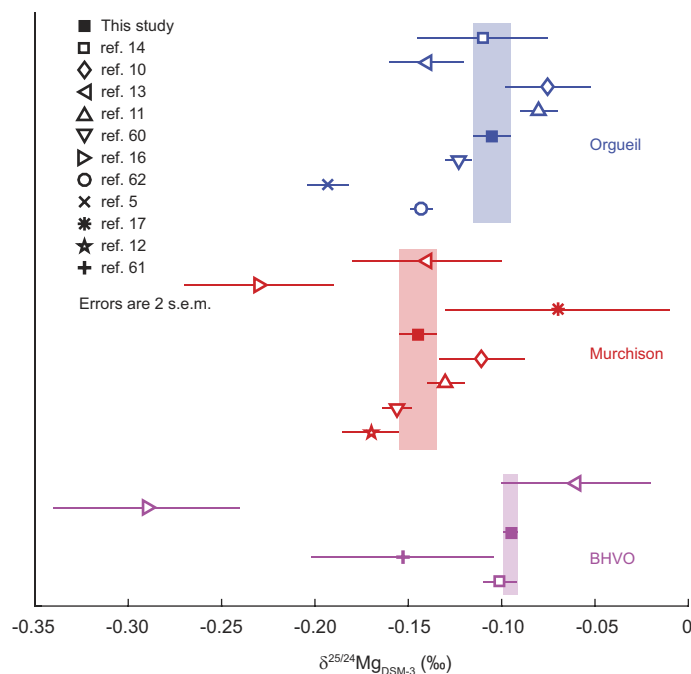
ratios are complicated by core formation because most Fe enters the core. In our model we assume that the iron in the core has not been affected by vaporization, inferred to occur later. For instance, the effect of ~48% Fe loss (**c**) on the current bulk silicate Earth Fe content is dependent on the fraction of Fe that entered the core before collisional vaporization and the oxygen fugacity evolution of the growing Earth. For reference, the datum labelled Fe\*\* in **d** is therefore the Fe/Ca of the bulk Earth (calculated from ref. 56) instead of the Fe/Ca of the bulk silicate Earth. Similarly, Si can also enter the core, although its quantity is likely to be <3 wt% (ref. 57). Right-pointing arrow in **a** indicates the effect of 3 wt% Si in the core (3,000 K assumed for metal–silicate Si isotope fractionation factor<sup>58</sup>).



#### Extended Data Figure 4 | Comparison between modelled compositions of a vapour depleted liquid and observed planetary compositions.

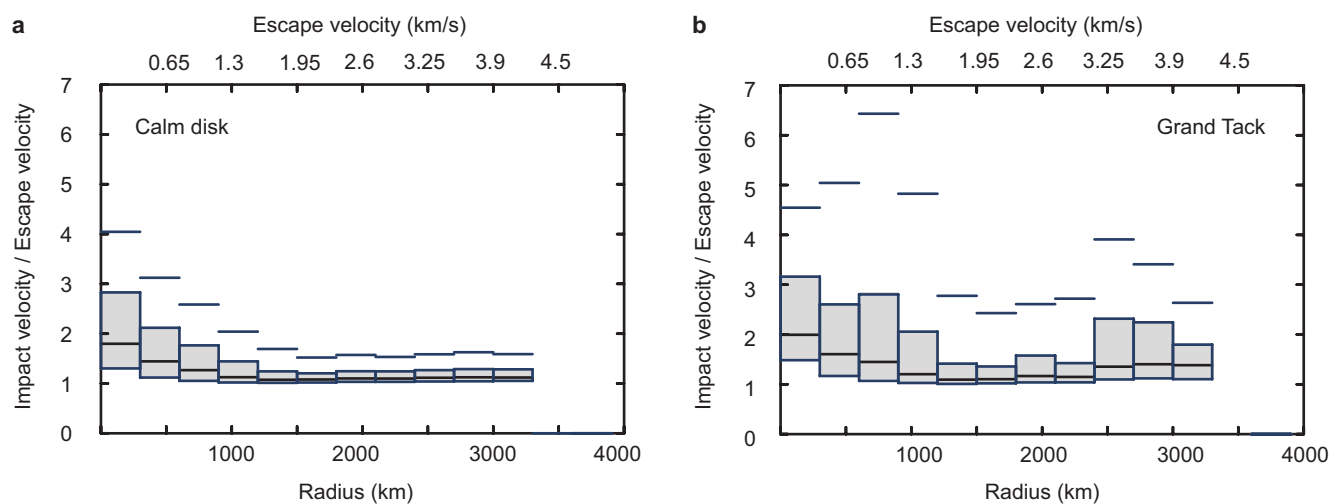
Similar to Extended Data Fig. 3, but for model runs with a CI chondrite initial composition. **a**, Modelled changes in isotope compositions ( $\text{‰}$  per AMU) against total relative vapour loss ( $F_{\text{Total}}$  in mole fractions). **b**, Observed isotope compositions relative to CI chondrites (errors are 2 s.e.m.). Note that observed Mg and Fe isotope compositions are presented relative to their chondritic mean, whereas Si isotope

observations are relative to a mean of carbonaceous and ordinary chondrites<sup>59</sup>, because those chondrites have indistinguishable Si isotope compositions, yet are distinctly different from enstatite chondrites (see ref. 4 and references therein). **c**, Loss (mole fraction) of a given element ( $X$ ),  $f_X$ , versus  $F_{\text{Total}}$ . **d**, Molar element/Ca ratio of the terrestrial mantle<sup>7</sup>, normalized to that of CI chondrites<sup>7</sup> ( $(X/\text{Ca})_{\text{CI}}$ ). As in Extended Data Fig. 3, Fe\*\* in **d** is the Fe/Ca of the bulk Earth.

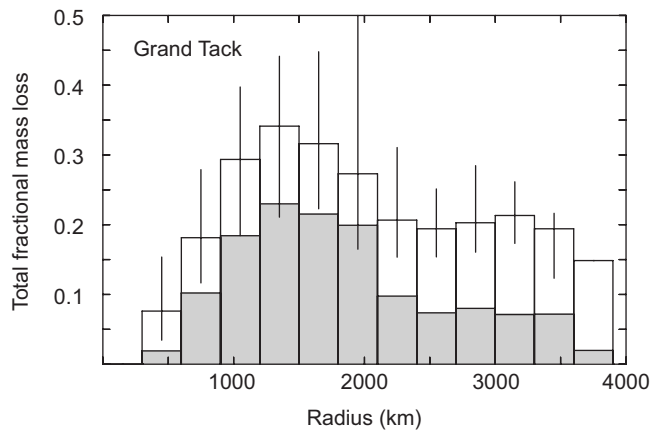


**Extended Data Figure 5 | Magnesium isotope compositions of reference samples analysed in multiple studies.** The shaded areas show the mean and 2 s.e.m. of the isotope compositions observed in this study. Data are from this study and refs 5, 10–14, 16, 17, 60–62. Note that the plotted composition of Murchison from ref. 10 is a mean of the two replicates presented in table 1 of ref. 10. The value for BHVO from ref. 16 is BHVO-1, all others are BHVO-2.





**Extended Data Figure 6 | Variation in velocity of individual impacts (normalized by target-body escape velocity) as a function of target body radius.** Central line denotes median value, shaded box encompasses the region spanning the 25th to 75th percentiles, upper lines denote the 90th percentile. Bulk density is assumed to be  $3,000 \text{ kg m}^{-3}$ .



**Extended Data Figure 7 | Fractional mass loss in the Grand Tack simulation as a function of final body radius for the direct vapour outflow model.** This illustrates results both with (white boxes, as Fig. 2b) and without (shaded boxes) the inclusion of inheritance effects (see Methods). Boxes denote the median value, bars denote the 25th and 75th percentiles.

**Extended Data Table 1 | Sample sources and weights of digested sample from which aliquots were taken for Mg isotope analysis in this study**

<i>Meteorites</i>	Source	Sample weight digested (mg)	Identification number
Orgueil	NMH	98.14	BM 36104
Ivuna	NHM	11.6	BM 1991, M5
Al Rais	NHM	4.6	BM 1971, 289
Renazzo	NHM	4.4	BM 41105
Kainsaz	NMH	69.34	BM 1988,M24
Murchison	NMH	86.92	BM 1970,6
Parnallee	NMH	6.37	BM 34792
Dhurmsala	NHM	12.69	BM 96262
Ceniceros	NMH	46.93	BM 1989,M31
Zag	Meteorite dealer	7.18*	-
Khairpur	NMH	69.39	BM 51366
Hvittis	NHM	45.8	BM 86754
Yilmia	NHM	29.8	BM 1972, 132
St Mark's	NMH	60.37	BM 1990, 339
Abee	NHM	66.7	BM 1997, M7
Indarch	NHM	97.0	BM 1921, 23
ALHA 77005	NASA	71.99	ALHA77 005, 234
DaG 476	Meteorite dealer	91.78	-
EETA 79001	NASA	121.19	EETA79 001, 665
RBT 04262	NASA	89.09	RBT 04 262, 61
Zagami	Meteorite dealer	61.00	-
LAR 06319	NASA	95.58	LAR 06 319, 59
Johnstown	NHM	133.31	BM 1959,828
Shalka	NHM	155.58	BM 33761
Tatahouine	NHM	112.89	BM1931,490
d'Orbigny	Meteorite dealer	15.28*	-
<i>Terrestrial</i>	Location		
BZ116	ref 63	7.89*	Bozu section, Horoman peridotite, Japan
Vi 313-102	ref 64	23.97*	Vitim volcanic field, Russia
BZ143	ref 63	4.23*	Bozu section, Horoman peridotite, Japan
BZ-29	ref 65	12.97*	Zabargad Island, Egypt
Vi 314-56	ref 64	10.39*	Vitim volcanic field, Russia
BZ251	ref 63	11.93*	Bozu section, Horoman peridotite, Japan
2370-1	ref 66	3.39	9-10°N East Pacific Rise
DS12-29	ref 67	3.92	26°S Mid-Atlantic Ridge
9/30a(1)	ref 68	2.07	57°E South-West Indian Ridge

NHM, Natural History Museum, London, UK; NASA, National Aeronautics and Space Administration.

\*Aliquot from a homogenized powder of several grams.